On Rotor Aeroacoustic Optimization for Urban Air Mobility

Olívia Raquel Leite Pinto
oliviapinto@tecnico.ulisboa.pt

Instituto Superior Técnico, Universidade de Lisboa, Portugal

April 2021

Abstract

This article presents an optimization study of the noise produced by rotors in the context of Urban Air Mobility. The importance of this study is based on the expected growth of Urban Air Mobility in larger cities across the globe and on the consequent effort to decrease the noise emitted by this type of aircraft. Provided that rotors constitute a major part of the noise produced by this aviation segment, given the fact that the aircraft are intended to be fully electric, the design of these components is of paramount importance for noise minimization. For the simulation accomplished within the optimization process, an open-source aerodynamic and aeroacoustic code (FLOWUnsteady, or FLight, Optimization, and Wind Unsteady) was integrated within an optimization module created specifically for the current work. These tools were based on the Formulation 1A of Farassat (PSU-WOPWOP) and the Brooks-Pope-Marcolini airfoil noise model (FLOWNoise), being utilized for the prediction of the tonal and atonal noise, respectively. The simulation code is applied to predict rotor noise which is posteriorly reduced by the means of an optimization algorithm, leading to the proposed optimal rotor design.
Keywords: Aeroacoustics, Noise Optimization, UAM, Rotors, Differential Evolutional Algorithms.

1. Introduction

By 2050, it is expected that over two thirds of the world's population lives in cities [1]. This increase on urbanization leads to a search for new means of transportation and solutions that not only sustain the increase of the number of passengers and cargo, but also the needs in terms of geographic coverage, speed and environmental efficiency [1]. UAM [2] is a proposed alternative to the classic means of transportation that could solve the stated problems, having the increasing congestion in cities as its primary market driver. It is important to underline that the proposed implementation of this type of mobility depends on the ability to minimize the noise generated by vertical take-off and landing (VTOL) aircraft for the UAM segment.

2. Background

2.1. Nature of rotor noise

The sources of rotor noise may be divided into two distinct groups: discrete frequency and broadband aerodynamic noise.

The discrete frequency noise comprises the deterministic components of thickness (due to the displacement of the fluid by the rotor blade), loading (caused by the accelerating force of the fluid generated by the moving blade), blade-vortex interaction (resultant of the interaction of a shed tip vortex with a following blade) and high-speed impulsive (associated with transonic flow around the blade) noises. Broadband noise is due to the association between the blade loading with turbulent flow on or near the blade's surface and consists of non-deterministic loading noise sources, comprising turbulence ingestion, blade-wake interaction and blade self-noise.

2.2. Formulation 1A of Farassat

Formulation 1A of Farassat [3] presents a solution to the Ffowcs Williams and Hawkings (FW-H) equation when the represented surfaces move at subsonic speeds. The FW-H comprises a generalization of the Lighthill's acoustic analogy approach, including the effects of general types of surfaces and motions [4]. Through the mathematical theory of distributions, FW-H were able to rearrange the Navier-Stokes equations into the form of an inhomogenous wave equation with a quadrupole source distribution in the volume surrounding the body and a monopole and dipole sources on the body's surface. In current days, the FW-H equation on the time-domain integral formulation is vastly used to predict deterministic rotor noise:

$$\Big(\frac{\partial^2}{\partial t^2} - c^2\frac{\partial^2}{\partial x_i^2}\Big)(\overline{\rho-\rho_0})$$
$$= \frac{\partial^2\overline{T_{ij}}}{\partial x_i \partial x_j} - \frac{\partial x}{\partial x_i}\Big(p_{ij}\delta(f)\frac{\partial f}{\partial x}\Big) + \frac{\partial}{\partial t}\Big(\rho_0 v_i \delta(f)\frac{\partial f}{\partial x_i}\Big), \quad (1)$$

where $\overline{\rho-\rho_0}$ is the generalized density perturbation (which constitutes a measure of the sound amplitude) and T_{ij} is a generalized function equal to Lighthill's stress tensor $T_{ij} = \rho u_i u_j + p_{ij} - c^2(\rho - \rho_0)\delta_{ij}$ outside any surfaces and zero within them. c represents the speed of sound, ρ the fluid density, p_{ij} the compressive stress tensor and v_n the normal velocity relative to the surface. Through inspection of equation 1, the objective will be to solve the thickness and the loading noise equations, represented, respectively, by:

$$\Box^2 p'_T = \frac{\delta}{\delta t}[\rho_0 v_n \delta(f)], \quad (2)$$

and

$$\Box^2 p'_L = -\frac{\delta}{\delta x_i}[p n_i \delta(f)], \quad (3)$$

where $\Box^2$ is the wave or D'Alembertian operator in the three dimensional space, being equal to $\Box^2 = (1/c^2)(\partial^2/\partial^2) - \nabla^2$, and $H(f)$ is the Heaviside function.

Formulation 1A of Farassat neglects the quadrupole sources, which are not significant in several subsonic applications, as in the rotor case studied. Via the use of algebraic derivation from equations 2 and 3, the thickness (p'_T) and loading (p'_L) noise components of Formulation 1A are obtained through:

$$4\pi p'_T(x,t) = \int_{f=0}\left[\frac{\rho_0 \dot{v}_n}{r(1-M_r)^2} + \frac{\rho_0 v_n \hat{r}_i \dot{M}_i}{r(1-M_r)^3}\right]_{ret} dS + \int_{f=0}\left[\frac{\rho_0 c v_n (M_r - M^2)}{r^2(1-M_r)^3}\right]_{ret} dS, \quad (4a)$$

and

$$4\pi p'_L(x,t) = \frac{1}{c}\int_{f=0}\left[\frac{\dot{l_r}}{r(1-M_r)^2}\right]_{ret} dS + \frac{1}{c}\int_{f=0}\Big[\frac{l_r(r\dot{M}_r + cM_r - cM^2)}{r^2(1-M_r)^3}\Big]_{ret} dS + \int_{f=0}\Big[\frac{l_r - l_M}{r^2(1-M_r^2)}\Big]_{ret} dS, \quad (4b)$$

respectively.

2.3. Brooks, Pope & Marcolini model

Broadband self-noise is the noise produced when an airfoil encounters smooth nonturbulent inflow.

The Brooks, Pope & Marcolini (BPM) airfoil noise model defines semi-empirical models for prediction of broadband self-noise, being initially defined for NACA 0012 [5]. The BPM model presents two major limitations, namely: the empirical nature of the equations and the fact that the boundary layer parameters are not appropriate for the generalization of airfoils, namely for cambered airfoils.

The five self-noise mechanisms, representing the interaction between the blade and the turbulence it induced, whose sound pressure levels were predicted by semi-empirical functions in the BPM method [6], are the following:

1. Turbulent boundary layer – trailing edge;
2. Separation stall;
3. Laminar boundary layer – vortex shedding;
4. Tip vortex;
5. Trailing-edge bluntness – vortex shedding.

The developed semi-empirical expressions for sound pressure noise prediction are only dependent on flow characteristics and on boundary layer parameters and can be generalized through the following expression:

$$SPL_i = 10\log\Big(\frac{\delta^* M^{f_i} dl \bar{D}_h}{r_e^2}\Big) + G_j(St) + G_i(Re), \quad (5)$$

where δ^* is the boundary layer displacement thickness on each side of the airfoil, M represents the Mach number, f_i is the raised power depending on the mechanism (with $i \in 1,2,3,4,5$), $\bar{D}_h$ is the directivity and r_e the source-observer distance. G are empirical functions representing the spectral shape, depending whether on the Strouhal number (St) or on the Reynolds number (Re). It should be taken into consideration that, for the trailing-edge bluntness vortex shedding, a slight variation in equation 5 occurs, where the shape functions will depend on the blunt thickness of the trailing edge h and on the solid angle between the suction and pressure sides of the airfoil, ψ.

3. Implementation

3.1. Dynamic Code

Upon the date of the making of the current work, the FLOWUnsteady software only had implemented a kinematic movement simulation. A *julia* module for the implementation of the dynamics for a quadcopter was created and connected to the FLOWUnsteady code in a partnership with Gabriele Bossotto [7], based on references [8, 9].

The implementation of the dynamic movement for the present time step consists on the updating of

the angular velocity vector ω by adding the angular acceleration multiplied by the time step. Similarly, for the angles in the body frame (θ) and their correspondent angular velocity ($\dot{\theta}$), linear velocity ($\dot{x}$) and linear acceleration ($\ddot{x}$), and for the position (x) and linear velocity ($\dot{x}$). The difference between ω and $\dot{\theta}$ should be denoted, since the first constitutes the angular velocity with the previously mentioned direction, whilst the second is the derivative of the yaw, pitch and roll.

The computation of the linear acceleration ($\ddot{x}$) in the inertial frame is based on Newton's law:

$$m\ddot{x} = \begin{bmatrix} 0 \\ 0 \\ -mg \end{bmatrix} + RT_B + F_D, \tag{6}$$

where g is the gravitational acceleration; T_B is the thrust in the body frame that is converted to the inertial frame by the rotation matrix (R) that goes from the body to the inertial frame, given by:

$$R = \begin{bmatrix} c_\phi c_\psi - c_\theta s_\phi s_\psi & -c_\psi s_\phi - c_\phi c_\theta s_\psi & s_\theta s_\phi \\ c_\theta c_\psi s_\psi & c_\phi c_\theta c_\psi - s_\phi s_\psi & -c_\psi s_\theta \\ s_\phi s_\theta & c_\phi s_\theta & c_\theta \end{bmatrix}; \tag{7}$$

F_D represents the global drag forces and is calculated by

$$F_D = \begin{bmatrix} -k_d \dot{x} \\ -k_d \dot{y} \\ -k_d \dot{z} \end{bmatrix}. \tag{8}$$

In equation 7, c and s represent the functions sine and cosine, respectively, and in equation 8, k_d is the friction constant and $\dot{x} = (\dot{x}, \dot{y}, \dot{z})^T$ the transposed velocity of the quadrotor in the inertial frame.

The total thrust (T_B) and external torque (τ_B) vectors in the body frame, are calculated in the following manner:

$$T_B = \sum_{i=1}^{4} T_i = k \begin{bmatrix} 0 \\ 0 \\ \sum \omega_i^2 \end{bmatrix}, \tag{9}$$

and

$$\tau_B = \begin{bmatrix} Lk(\Omega_1^2 - \Omega_3^2) \\ Lk(\Omega_2^2 - \Omega_4^2) \\ b(\Omega_1^2 - \Omega_2^2 + \Omega_3^2 - \Omega_4^{2s}) \end{bmatrix}, \tag{10}$$

respectively.

In equation 9, k represents an adequately proportional constant and T_i the torque in the inertial frame. In equation 10, L is the distance from the quadcopter's centre to any of its propellers geometric centre, and ω the angular velocity vector (pointing along the axis of rotation). This simplified model was applied in order to facilitate the simulation, not taking into consideration several nonlinear effects, such as blade flapping, rotational drag forces and the effects of the wind, amongst others.

In both the equations 9 and 10, the index i and the numeration replacing it represent each one of the four rotors, as depicted in figure 1.

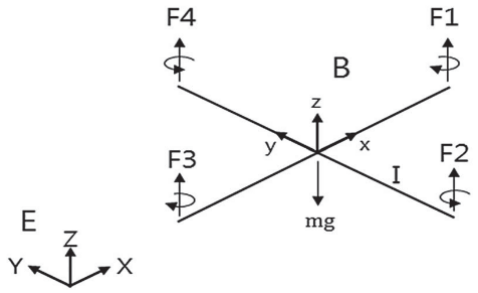

Figure 1: Quadrotor body and inertial frames [9].

The angular acceleration vector $\dot{\omega}$ is given by:

$$\dot{\Omega} = \begin{bmatrix} \dot{\Omega}_x \\ \dot{\Omega}_y \\ \dot{\Omega}_z \end{bmatrix} = I^{-1}(\tau - \Omega \times (I\Omega)), \tag{11}$$

where the quadcopter's inertia matrix I is given by

$$I = \begin{bmatrix} I_{xx} & 0 & 0 \\ 0 & I_{yy} & 0 \\ 0 & 0 & I_{zz} \end{bmatrix}, \tag{12}$$

and τ consists on the vector of external torques.

The angular velocity vector $\dot{\theta}$ is computed using:

$$\dot{\theta} = \begin{bmatrix} 1 & 0 & -s_\theta \\ 0 & c_\phi & c_\theta s_\phi \\ 0 & -s_\phi & c_\theta c_\phi \end{bmatrix}^{-1} \Omega. \tag{13}$$

3.2. Evolutionary Algorithms

Evolutionary algorithms are based on processes that occur in nature or in society. Their vast majority is population-based and derivative-free, enclosing several optimization algorithms, such as differential evolution (DE), evolution strategies (ES), genetic algorithms (GA), and evolutionary programming (EP) [10].

In DE, the initial population is randomly generated accordingly to a normal or uniform distribution. After this process of initialization, the algorithm enters a loop consisting in the evolutionary operations of mutation, crossover and selection. This loop occurs until either the algorithm converges to the true optimum solution or a certain termination criterion is fulfilled, such as the arrival to a maximum iteration/time or the reach of a maximum number of generations.

There are different possible strategies of DE based on the vector to be perturbed, the number of different vectors considered for perturbation and

the type of crossover used. Price & Storn [11] proposed ten different strategies following the nomenclature $DE/x/y/z$, where x represents the string of the vector to be perturbed (which can either occur only in the *best* vector of the previous generation, or in any random, *rand*, vector), y the number of vectors of x considered for perturbation, and z the type of crossover used.

3.3. Optimization Framework Description

In the present optimization, a basis rotor was studied when performing a hover flight at 4000 rpm. An optimization code, in order to decrease the rotor's noise emissions, was developed, with the aim at obtaining an acoustically optimized blade geometry.

Firstly, a plane rotor is created within the simulation providing the optimizer module with a simple non-optimized geometry as its starting point, which may be observed in figure 2.

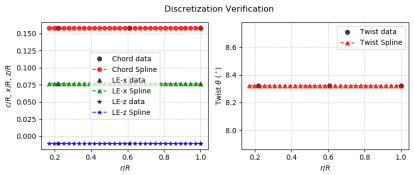

Figure 2: Geometry of the basis rotor.

The basis rotor will undergo an optimization process of its geometry through a b-spline interpolation, of a chosen polynomial degree k, of the values of the design variables at a chosen number of n points along the span of the rotor. The design parameters chosen were the tip radius (R_{tip}), the chord (c) and the twist distribution (θ) along the rotor's span, and the distributions of the height (LE_z) (from the top of the rotor) and the sweep (LE_x) of leading edge along the span of the rotor. These design variables were altered within the loop of the optimization code, in the limits presented in table 3.3. This practice of the use of splines along a rotor blade's span constitutes a commonly used technique with optimizations involving shapes that very often lead to a decrease of the computational cost with little loss in the model parameterization fidelity [12].

Since the main goal of a rotor is to provide thrust, it should be considered as a constraint, thus introducing the component of performance in the optimization code. In the case of the thrust of the current iteration ($T_{current}$) being smaller than the minimum ($T_{minimum}$) allowed by the code, an indirect method was chosen, where a penalty on the objective function was imposed.

In case of the algorithm passing the thrust constraint, the tonal and broadband overall sound pressure levels (OASPL) in dB are respectively computed via the use of the PSU-WOPWOP binary [13] through the implementation of Formulation 1A of FW-H and the FLOWBPM package [14] through the implementation of the BPM semi-empirical equations, and added together. The adding procedure is done by converting each tonal and broadband OASPL at a given frequency to its corresponding root mean square pressure, adding them together, and converting the result back into decibels. A total of 360 microphones are simulated circularly surrounding the rotor, equally spaced at a 90^o degree rotation plane relatively to the rotor's plane, each measuring the OASPL value registered at its own position. As the simulated OASPLs cannot be directly optimized since the method available within the optimization package provided, namely BlackBoxOptim [15], only allows for the optimization of a scalar, the EAOASPL was chosen as a metric for the optimization process. This metric consists in a logarithmic average of the OASPL measured by each microphone, therefore taking into account both tonal and broadband noises, and is given by the following equation:

Table 1: Design constraints of the optimization code.

Design variable	Lower bound	Upper bound
$R_{tip}(m)$	0.10624	0.1
c	0.03	0.30
θ (degrees)	5.00	26.00
LE_z/R_{tip}	-0.03	0.05
LE_x/R_{tip}	0.00	0.30
T	1	1

$$\text{EAOASPL} = 10 \log \sum_{i=1}^{N} 10^{\frac{OASPL(i)}{10}} \quad , \tag{14}$$

where $OASPL(i)$ is the value of OASPL registered in the $i-th$ microphone of the simulated sphere, and N is the number of data points across the surface of the aeroacoustic sphere, which in the case implemented, corresponds to the 360 microphones previously mentioned.

The mathematical formulation of the described optimization problem is resumed in equation 15:

$$\begin{aligned} &\text{minimize} && f\,(\mathrm{x}) = 10 \log \sum_{i=1}^{N} 10^{\frac{OASPL(i)}{10}} \\ &\text{with respect to} && \mathrm{x} = R_{tip},\ \mathrm{c},\ \theta, LE_z, LE_x \\ &\text{subject to} && \mathrm{c} = T_{minimum} - T_{current} \leq 0 \end{aligned} \quad , \tag{15}$$

and a flowchart illustrating the described code is presented in figure 3.

Taking into consideration the absence of a definition of a single expression for the objective function (bearing in mind that the EAOASPL uses the OASPL values that rely on intricate expressions), a gradient-free method must be used. Within gradient-free methods, an adaptive differential evolution method was chosen to be applied in the optimization process given that, when there might exist multiple local optima, as in the present case, evolutionary algorithms become a preferable solution, as they allow the exploration of all parts of the feasible design space [16]. The method chosen was the $DE/rand/1/bin$, as it is considered to be the most successful method comprised in adaptive differential evolution [17].

3.4. Verification and Validation

The validation of the FLOWUnsteady software [18] was tested against results obtained in the aeroacoustic tunnel of the aerospacial laboratory of Instituto Superior Técnico by Gabriele Bossotto in [7]. These results are of particular importance regarding the validation of the optimization results, since the rotor utilized within the process is of similar dimensions of the rotor used for the optimization processes (both with a radius at its blade's tip of 0.18 meters).

For a rpm of 4000 (equal to the one used in the performed optimizations), FLOWUnsteady managed to follow the experimental SPL trend, with the first BPF being well captured at both angles of the microphones tested (of 0^{o} and -45^{o}) - as presented in figures 4(a) and 4(b). It is worth to note that although a peak between 7560 and 7570 Hz that is not predicted by the FLOWUnsteady software is noticeable within these figures. This is believed not to be correlated with a misprediction of the software since it should mainly due to the noise produced by the electric motor utilized in the experimental procedure that was not manageable to be subtracted when obtaining the rotor's noise (acquired through the subtraction of the background's and motor's noises to the total noise measured in the microphones). For an observer at 0^{o}, a greater deviation between the experimental and computational values is presented, possibly related to an underestimation of the thickness noise.

4. Results

4.1. Optimized Blade

The blade that suffered the greatest reduction in EAOASPL was obtained when performing a two point second order spline (the geometry of which is represented in figure 5). This blade obtained a 10.71dB decrease in the EAOASPL, when compared with the non-optimized blade, mainly due to the reduction of the loading noise achieved by the loosening of the thrust constraint in the optimization code and by allowing it to reach lower values than the one obtained by the performance of the basis blade (from approximately 3N to over 1N). The mentioned EAOASPL reduction is further represented in figure 8(a), where a comparison between the original and the optimized OASPL is presented.

The components of the OASPL of the basis and the optimized rotor were decomposed into their frequency and broadband components, so that their importance could be depicted. Firstly, the tonal noise components of the OASPL, namely the loading and the thickness noises were studied, as presented in figures 8(b) and 8(c), respectively. The first constitutes the largest component of the OASPL, being mainly propagated in the perpendicular direction, whilst the second is mainly propagated in an oblique direction. In this manner, for the in-plane microphone positions, thickness noise will dominate the pressure-time history, whereas for observers above or below the rotor tip-plane, steady thrust becomes the dominant contributor to the measured noise (that is, the loading noise will be higher at these positions), whilst the thickness noise is lessened.

Regarding the results obtained for the loading noise, due to the thrust constraint being inferior to the thrust of the basis blade, it is expected that figure 8(b) presents a significant reduction in the loading noise for the optimized blade, as it does.

In terms of broadband noise, this component presents the lowest pressure levels, as depicted in figure 8(d), as in the current simulation conditions it is mainly composed by laminar boundary layer vortex shedding and tip vortex formation noise, components that are intensified during descending flight, whereas the optimization is performed during hover, fact that explains the smaller values it presents, when in comparison with the frequency components of the noise.

4.2. Numerical Study

Several numerical studies were performed for different values of spline parameters, the results of which are present in table 2. From further inspection of table 2, the cases of $n2k1$, $n5k1$, and $n6k2$ appear to be close to an optima, having reached the value of the minimum thrust imposed by the ruling optimization constraint, that is, having reached thrust values close to the 1N thrust constraint imposed. These cases will be further analysed in order to study the influence of the design variables on the noise produced by the optimized rotor.

4.3. Comparison between cases: n2k1, n5k1 and n6k2

The geometry for the cases of $n2k1$, $n5k1$, and $n6k2$ which is presented in figures 5, 6 and 7, respectively, and the values obtained for the radius at the tip of

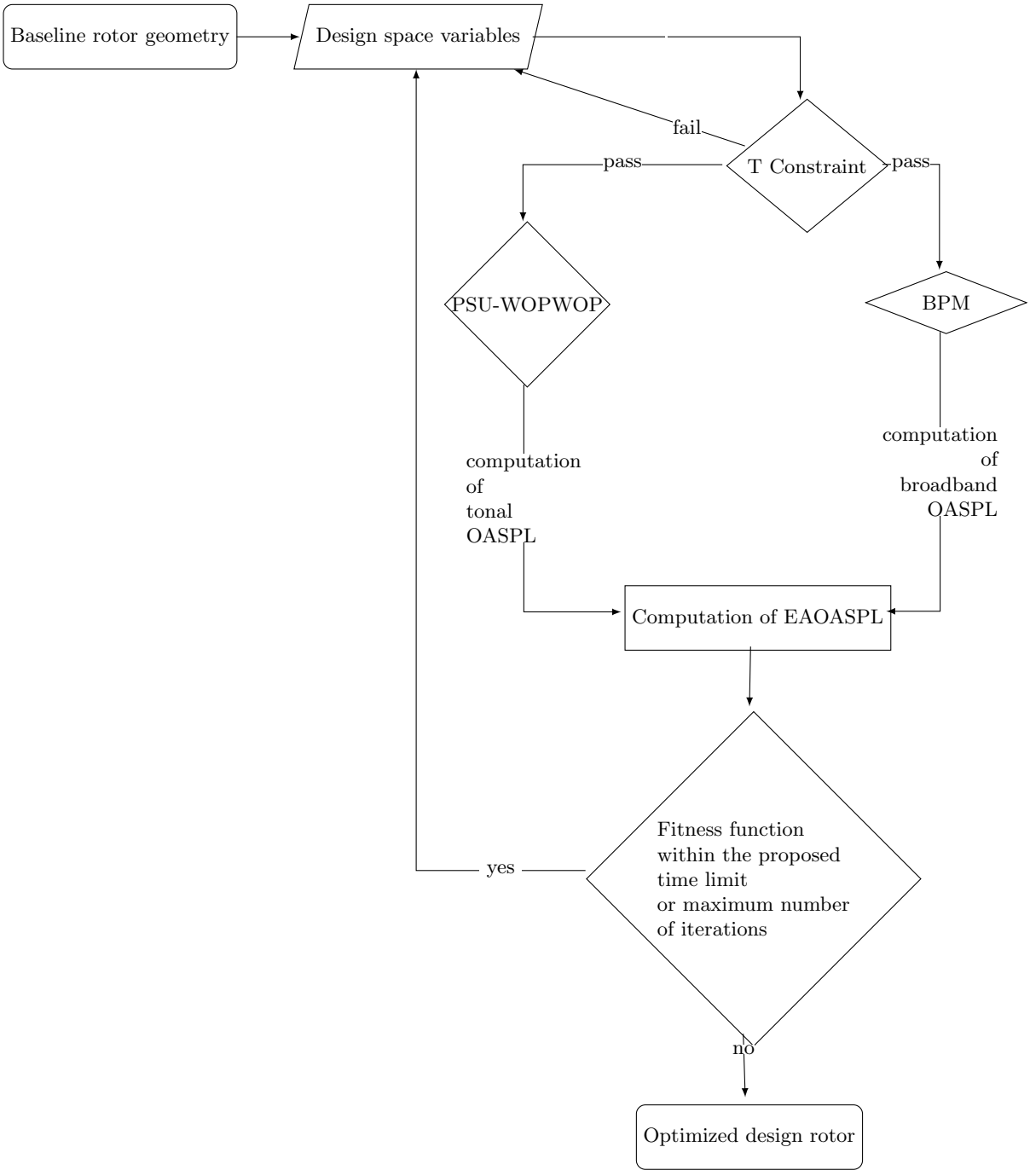

Figure 3: Flowchart of the optimization code.

Table 2: Optimization results.

Case	Total Number of Iterations	Best Iteration	EAOASPL (dB)	Thrust (N)
Basis blade	-	-	66.08	3.62
$n2k1$	188	17	55.37	1.03
$n3k1$	0	-	-	-
$n3k2$	27	22	63.4	2.24
$n4k1$	47	17	65.00	2.22
$n4k2$	6	2	57.02	1.24
$n4k3$	35	34	60.00	1.49
$n5k1$	109	39	55.50	1.05
$n5k2$	90	9	57.86	1.12
$n5k3$	17	9	58.84	1.63
$n5k4$	25	22	65.39	2.24
$n6k1$	11	8	58.47	1.50
$n6k2$	105	63	56.67	1.14
$n6k3$	11	-	-	-
$n6k4$	1	-	-	-
$n6k5$	22	2	62.06	1.38

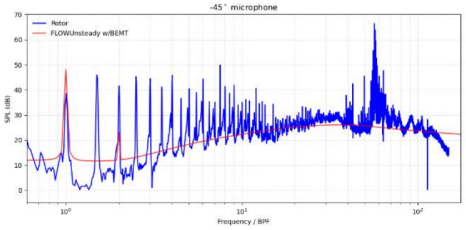

(a) Experimental and computational (FLOWUnsteady with Blade Element Momentum Theory) SPL comparison for an observer at $-45°$.

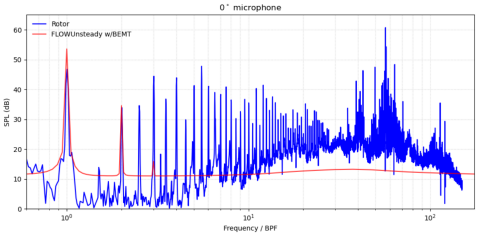

(b) Experimental and computational (FLOWUnsteady with Blade Element Momentum Theory) SPL comparison for an observer at 0°.

Figure 4: SPL (dB) obtained for an observer at a 90^{o} plane with the rotor's vertical axis, positioned at 2.3 meters distance from the rotor's hub, for a rotor in hover at 4000 rpm [7].

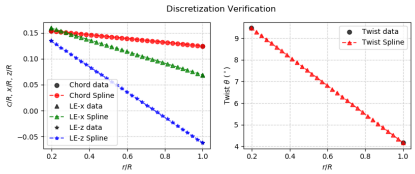

(a) Geometric discretization of the optimized 2 point first order spline two-bladed rotor.

(b) 3D representation of the optimized rotor.

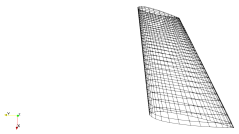

(c) Contour of the 2 point first order two-bladed optimized rotor.

Figure 5: Geometry of the optimized rotor.

the blades for mentioned cases, which are presented in table 3, will further help to explain the variations in the different types of studied noises. Regarding the obtained design variables, from the inspection of both figures 2 and 9(b), it is observable that for all the cases studied, a reduction of the radius at the tip of the blade was associated with a reduction of the loading noise; the pitch parameter further helped the reduction of this type of noise (as can be seen in figures 5(a), 6(a), and 7(a)), since it influenced the spanwise inflow distribution and, consequently, the aerodynamic forces. The thickness component of the noise increased with the volume of the analysed blade (depicted in figures 5(a), 6(a), 7(a), and 9(a)). Concerning the sweep of the blade, this parameter did not present a great influence on the results obtained due to the low velocity of the simulations performed (below Mach 0.5). With respect to the broadband component of the noise (present in figure 9(c)), the twist parameter lead to a decrease of this type of noise, with a translation of the aerodynamic forces towards the inwards of the blade and the consequent reduction of the broadband noise generated by vortex roll-up.

Table 3: Optimization results.

Case	Rtip (m)
Basis blade	0.177775
$n2k1$	0.153152
$n5k1$	0.121984
$n6k2$	0.104620

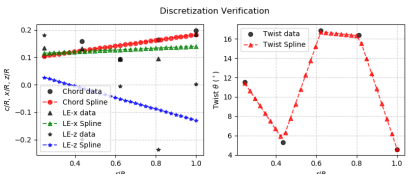

(a) Geometric discretization of the optimized 5 point blade first order spline two-bladed rotor.

(b) 3D representation of the optimized 5 point blade first order spline two-bladed rotor.

(c) Contour of the optimized 5 point blade first order spline two-bladed rotor.

Figure 6: Geometry of rotor with an $n5k1$ spline optimization.

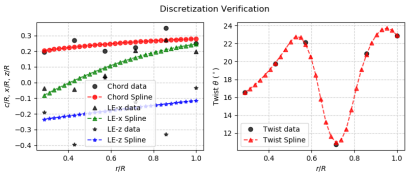

(a) Geometric discretization of the optimized 6 point blade second order spline two-bladed rotor.

(b) 3D representation of the optimized 6 point blade second order spline two-bladed rotor.

(c) Contour of the optimized 6 point blade second order spline two-bladed rotor.

Figure 7: Geometry of rotor with an $n6k2$ spline optimization.

4.4. Population study

The higher the number of individuals, the higher the variation within the population, and the higher the number of new vectors introduced per iteration, providing more variability. Although the positive consequences enumerated derived from a high number of individuals in the population, it also leads to an increase of the computational effort. In order to study both of the enumerated effects, the optimization of the basis blade with a two point second order polynomial was studied for a population of 50, 100 and 150 individuals, having obtained no major impact on the studied cases, with a variation of the EAOASPL lower than 1.5% amongst them. This result implies that the parameters chosen for the bimodal distributions for the setting of the next generation's mutation factor, F, and crossover rate, CR, values were well-adjusted, introducing enough variation into a 50-individual population in order for it to achieve results as good as the ones obtained with an 100 or 150 population. This result leads to a more efficient optimization, saving computational effort, since smaller populations need shorter optimization times.

4.4.1 Parametric study on the effect of the number of blades

A study of the effect of the number of blades on noise optimization was obtained through the optimization of two-blade, three-blade, and four-blade rotors for a $n2k1$ spline along their span. Similar EAOASPL's were obtained for the three studied cases, as presented in table 4. Increasing the number of blades leads to an increase in the thickness noise that was compensated by a reduction of the chord in the optimizations for higher numbers of blades. The loading noise was similar between the simulations since its decrease provided by increasing the number of blades was contradicted by the previously mentioned chord reduction.

Table 4: Optimization results: study of the effect of the number of blades on the rotor optimization process.

Case	Number of blades	EAOASPL (dB)
Basis blade	2	66.08
$n2k1$	2	55.37
$n2k1$	3	55.06
$n2k1$	4	55.32

5. Conclusions

The main objective accomplished with the current work was the creation of an optimization tool capable of reducing the noise produced by a rotor, that responded to the increasingly demanding noise constraints of the UAM segment. In such a manner, the optimization module created successfully integrates an aeroacoustic simulator, providing a tool capable to perform the optimization of a rotor geometry on an initial design phase in terms of the OASPL it produces.

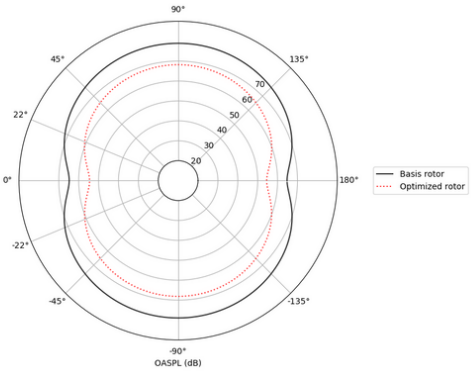

(a) Optimization OASPL (dB) of the optimized blade.

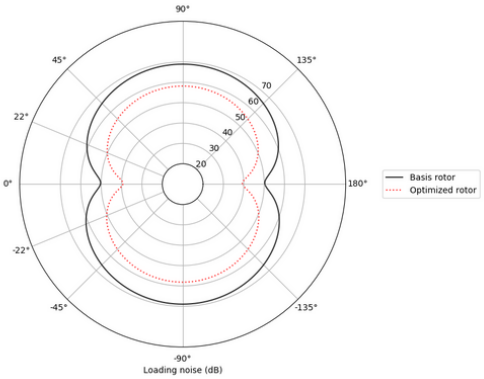

(b) Loading noise (dB) of the optimized blade.

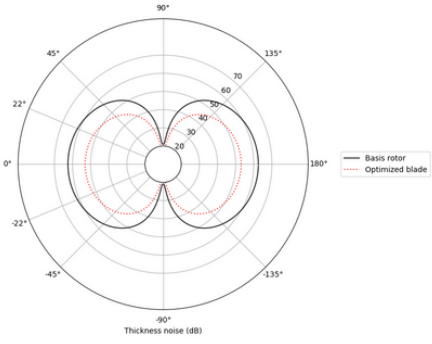

(c) Thickness noise (dB) of the optimized blade.

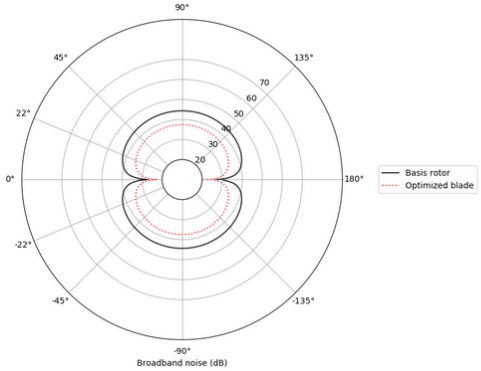

(d) Broadband noise (dB) of the optimized blade.

Figure 8: Geometry of the optimized rotor.

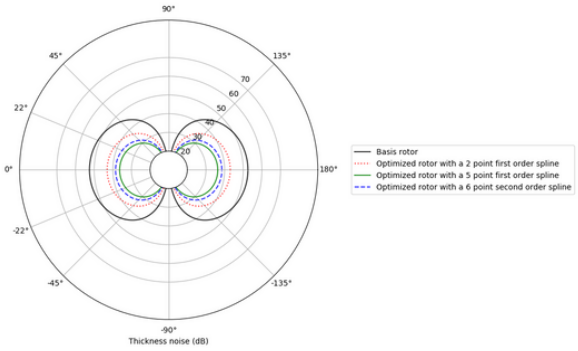

(a) Thickness noise of the optimized blades (dB).

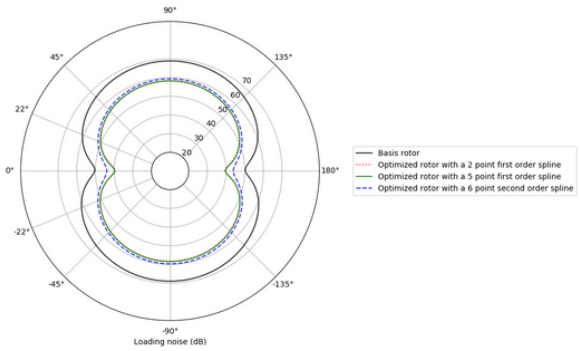

(b) Loading noise (dB) of the optimized blades.

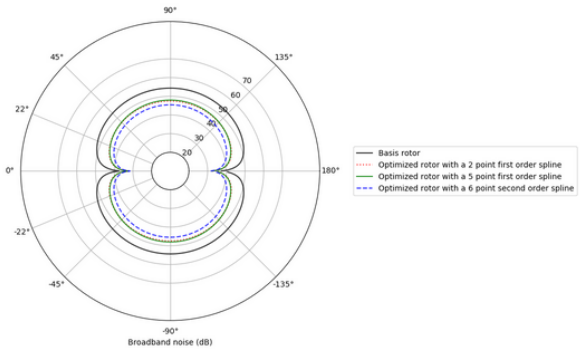

(c) Broadband noise (dB) of the optimized blades.

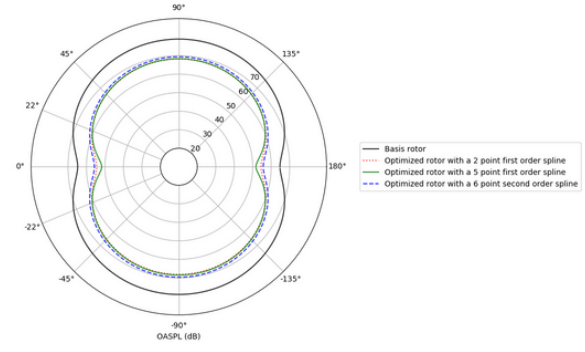

(d) OASPL noise (dB) of the optimized blades.

Figure 9: Noise results of the optimized blades.

References

[1] Parker D. Vascik. Systems analysis of urban air mobility operational scaling. Technical Report ICAT-2020-02, MIT International Center for Air Transportation, February 2020.

[2] Anna Straubinger, Raoul Rothfeld, Michael Shamiyeh, Kai-Daniel Büchter, Jochen Kaiser, and Kay Olaf Plötner. An overview of current research and developments in urban air mobility – Setting the scene for UAM introduction. *Journal of Air Transport Management*, 87:101852, August 2020.

[3] F. Farassat. Derivation of $f$ormulations 1 and 1a of $f$arassat. Technical Memorandum 214853, NASA, March 2007.

[4] J. E. Ffwocks Williams and D. L. Hawkings. Sound generation by turbulence and surfaces in arbitrary motion. *Philosophical Transactions of the Royal Society of London*, 264(1151):321–342, May 1969.

[5] Pietro Bortolotti, Emmanuel Branlard, Andy Platt, Patrick J. Moriarty, Carlo Sucameli, and Carlo L. Bottasso. Aeroacoustics noise model of openfast. Technical report, National Renewable Energy Laboratory, August 2020.

[6] Thomas F. Brookes, D. Stuart Pope, and Michael A. Marcolini. Airfoil self-noise and prediction. *NASA Reference Publication*, (1218), July 1989.

[7] Gabriele Bossotto. Urban air vehicle implementation and limitations - development of a new acoustic tool for noise prediction. Thesis to obtain the master of science degree in aerospace engineering, Instituto Superior Técnico de Lisboa, October 2021.

[8] Jose Carlos Lopez. Quadcopter simulation. https://engineering.usu.edu/students/clubs/shpe/quacopter-simulation.

[9] Jaehyun Yoon and Jongsoo Lee. Altitude and roll control of a hovering quad-rotor air vehicle using the multi-objective approximate optimization of proportional–integral–differential control. *Engineering Optimization*, 49(10):1704–1718, October 2017. (Accessed on 07/11/2021).

[10] J Zhang and A C Sanderson. *Adaptive Differential Evolution A Robust Approach to Multimodal Problem Optimization*, volume 1. Springer, 1st edition, 2009.

[11] Rainer Storn and Kenneth Price. Differential evolution: A simple and efficient adaptive scheme for global optimization over continuous spaces. *Journal of Global Optimization*, 23, 01 1995.

[12] Joaquim Martins and Andrew Ning. *Engineering Design Optimization*. 10 2021.

[13] Kenneth Brentner. Psu-wopwop computational aeroacoustic analysis. https://sites.psu.edu/wopwop/, 2021. (Accessed on 2 October 2021).

[14] byuflowlab BPM. https://github.com/byuflowlab/BPM.jl, 2021. (Accessed on 20 September 2021).

[15] Blackboxoptim. https://github.com/robertfeldt/BlackBoxOptim.jl, 2021. (Accessed on 2 October 2021).

[16] Lance Chambers, editor. *The practical handbook of genetic algorithms: applications*. Chapman & Hall/CRC, Boca Raton, Fla, 2nd ed edition, 2001.

[17] B.V. Babu and M.M.L. Jehan. Differential evolution for multi-objective optimization. In *The 2003 Congress on Evolutionary Computation, 2003. CEC '03.*, volume 4, pages 2696–2703 Vol.4, 2003.

[18] Eduardo Alvarez, Austin Schenk, Tyler Critchfield, and Andrew Ning. Rotor-on-rotor aeroacoustic interactions of multirotor in hover. *Brigham Young University Faculty Publications*, (4053), 2020.